



Title	Numerical flow visualization of a single large-sized bubble in turbulent Couette flow using OpenFOAM
Author(s)	Kim, Sangwon; Oshima, Nobuyuki; Park, Hyun Jin
Citation	Journal of visualization, 25(6), 1209-1225 https://doi.org/10.1007/s12650-022-00850-x
Issue Date	2022-12
Doc URL	http://hdl.handle.net/2115/89812
Rights	This version of the article has been accepted for publication, after peer review (when applicable) and is subject to Springer Nature 's AM terms of use, but is not the Version of Record and does not reflect post-acceptance improvements, or any corrections. The Version of Record is available online at: http://dx.doi.org/10.1007/s12650-022-00850-x
Type	article (author version)
File Information	Manuscript_JOV_20220505.pdf



[Instructions for use](#)

1 **Numerical flow visualization of a single large-sized bubble in turbulent**
2 **Couette flow using *OpenFOAM***

3

4 Sangwon Kim ^a, Nobuyuki Oshima ^b, Hyun Jin Park ^c

5

6 ^a *RIKEN Center for Computational Science, RIKEN, Kobe, Japan*

7 ^b *Computational Fluid Mechanics Laboratory, Faculty of Engineering, Hokkaido University,*
8 *Sapporo, Japan*

9 ^c *Laboratory for Flow Control, Faculty of Engineering, Hokkaido University, Sapporo, Japan*

10

11

12 *Corresponding Author:*

13 *Sangwon Kim, Ph.D.*

14 *RIKEN Center for Computational Science, RIKEN*

15 *7 Chome-1-26, Minatojima, Minamimachi, Chuo Ward, Kobe, Hyogo, 650-0047, Japan*

16 *Tel: +81-70-1546-7449*

17 *Fax: +81-11-706-6724*

18 *E-mail: sangwon.kim@riken.jp*

19

20

21

22

23

24 **Abstract**

25 Owing to different flow conditions—for example, Poiseuille and Couette flow—one could expect different
26 deformations of large-sized bubbles; however, bubble dynamics has been mostly investigated in channel flow.
27 Consequently, an intermediate flow condition shared by both the channel and ship surface is needed for large-
28 sized bubbles, although it can be difficult to simultaneously generate turbulent Couette flow in the channel and
29 measure the shear stress on the ship’s surface experimentally. In this study, large-sized bubbles in turbulent
30 Couette flow were investigated numerically to determine their common characteristics under such flow conditions.
31 The *interIsoFoam* solver from *OpenFOAM*—which can directly capture the interface via the geometric volume
32 of fluid method—was used to conduct the simulations of the gas–liquid interface problem. The turbulent Couette
33 flow was driven by top wall velocity condition with an initial perturbation, and three different bubble sizes with
34 Weber numbers in the range of 200–300 were chosen to determine the characteristics of large-sized bubbles. By
35 monitoring the results according to bubble size, we could determine bubble characteristics that were
36 distinguishable from those in turbulent Poiseuille flow. Consequently, bubble deformation was dominated by the
37 velocity gradient and shear rate, which was greater than that during single-phase flow from the liquid-film region.
38 These results allowed us to generalize the deformation mechanism of large-sized bubbles in turbulent Couette
39 flow into five categories—namely, the initial shape, deformation on the front side, change of the center of gravity,
40 pinch-off/breaking of the ligament, and deformation to a stable shape.

41

42 Keywords: Two-phase flow, large-sized bubble, turbulent Couette flow, direct numerical simulation, *OpenFOAM*

43

44 1. Introduction

45 Large-sized bubbles—that is, those larger than 1 mm in diameter—have attracted industrial attention as
46 components for air lubrication systems designed to reduce the drag of ships, as they are easier and less expensive
47 to generate than microbubbles (McCormick and Bhattacharyya, 1973; Madavan *et al.*, 1985; Merkle and Deustch,
48 1992; Kodama *et al.*, 2000) and air film methods (Fukuda *et al.*, 1999; Katsui *et al.*, 2003; Mäkiharju *et al.*, 2013).
49 The idea of using large-sized bubbles arose because the air injected along a ship’s bottom surface tends to form
50 millimeter-sized bubbles owing to the balance between the strong shear of the boundary layer and the surface
51 tension of the bubbles (Hinze, 1955; Sanders *et al.*, 2006; Johansen *et al.*, 2010). Murai *et al.* (2006) reported that
52 large-sized bubbles provided a velocity gradient that calmed the wake region. The performance of large-sized
53 bubbles for bubble drag reduction (BDR) was later found to depend on the bubble length (Murai *et al.*, 2007;
54 Oishi and Murai, 2014). In addition to the velocity gradient in the wake region, the liquid film between the bubbles
55 and wall was found to reduce skin friction by relaminarizing the flow in the film. From this viewpoint, Park *et al.*
56 (2019) experimentally investigated the relationship between film thickness and BDR. The physical mechanism of
57 the large-sized bubble drag reduction effect originates from its deformation, which can be induced by complex
58 parameters such as the shear stress around the bubble and its buoyancy. Murai (2014) reported additional details
59 regarding flow physics.

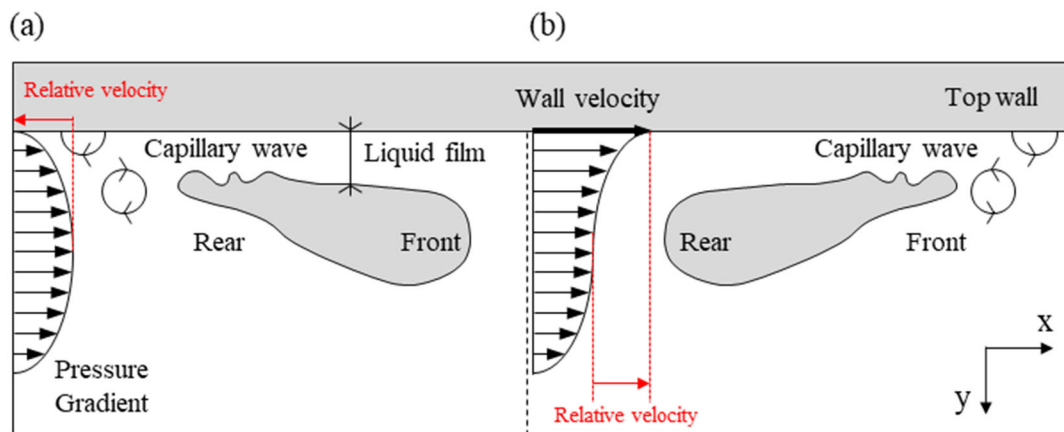
60 These BDR studies in horizontal flow were conducted in a horizontal channel to investigate the bubble
61 flow characteristics or control parameters of BDR (Park *et al.*, 2009, 2015, 2022; Tanaka *et al.*, 2021), as well as
62 in model ship tests to find an effective BDR condition for practical applications (Park *et al.*, 2016, 2018; Tanaka
63 *et al.*, 2020). In applying our understanding vis-à-vis air bubbles in horizontal channel flow to ship air lubrication
64 systems, it would be necessary to consider the difference in flow conditions between the horizontal channel and
65 ships because the driving principles of these flows are different—for example, horizontal channel flow, or
66 Poiseuille flow, is induced by pressure gradients, as shown in **Fig. 1(a)**, whereas a ship’s surface flow, or Couette
67 flow, is induced by the wall velocity, as shown in **Fig. 1(b)**.

68 These two different flow conditions are also controversial in single-phase flow and have been previously
69 studied in horizontal turbulent channel flow (Orlandi *et al.*, 2015; Andreolli *et al.*, 2021). Bubble characteristics
70 in these flows can differ, especially those of deformable bubbles. A comparison between bubble characteristics
71 under these two different flow conditions in the same flow domain—such as the horizontal channel condition—
72 could be used to explain any unclear aspect. Meanwhile, several problems in generating turbulent Couette flow
73 have been observed in experiments on horizontal channel flow. Turbulent Couette flow generation requires a long

74 channel and a complicated instrument for moving walls—such as a conveyor belt—which can hinder the
 75 measurement of the skin friction of the top wall. Consequently, most of the Couette flow for two-phase flow is
 76 laminar and driven by the motion of the top and bottom walls (Müller-Fischer *et al.*, 2008), this phenomena have
 77 been investigated using other methods—such as the Taylor–Couette flow method—on microbubbles, which have
 78 relatively small buoyancy forces (Fokoua *et al.*, 2015; Murai *et al.*, 2008, 2018).

79 However, a large-sized bubble has a high buoyancy force, which is important in determining its shape.
 80 For instance, the direction of the buoyancy force is in the spanwise direction of the flow in the Taylor–Couette
 81 flow model, while it is in the wall-normal direction in channel flow. Consequently, it can be difficult to identify
 82 the same characteristics observable in channel flow under Taylor–Couette flow conditions. These problems in
 83 generating turbulent Couette flow in a horizontal channel can be solved via numerical simulation because Couette
 84 flow is mathematically simpler than Poiseuille flow. In the present study, a direct numerical simulation of
 85 turbulent Couette flow with a single large-sized bubble of varying size was performed to examine the bubble
 86 characteristics—such as deformation and flow—inside the liquid film.

87



88

89 **Fig. 1** Schematic of large-sized bubble formation under different flow conditions, (a) turbulent Poiseuille flow,
 90 (b) turbulent Couette flow.

91

92 **2. Characteristics of a large-sized bubble and domain description**

93 A schematic of large-sized bubble formation under Poiseuille and Couette flow conditions is shown in **Fig. 1**.
 94 Generally, the surrounding of a single large-sized bubble under horizontal turbulent flow can be divided into the
 95 liquid film between the wall and bubble, the capillary wave on the bubble surface at the rear of the liquid film, the
 96 secondary flow from the bubble wake, and the bubble shape between the front and rear sides. Herein, bubble
 97 characteristics under Couette flow can be expected to form in opposite directions than under Poiseuille flow owing
 98 to the direction of the relative velocity from the center of the channel with respect to the wall velocity.

99 The experimental channel setup of Oishi and Murai (2014) is shown in **Fig. 2(a)**. The test section is 6000
100 mm in length, and a fully developed boundary layer is generated before the bubble is injected into the channel.
101 The channel width is 100 mm to prevent the effect of the interaction between the boundary layer and the sidewall.
102 In this study, the flow geometry and coordinate system of the numerical simulation is as shown in **Fig. 2(b)**; the
103 length and width of the computational domain can be shortened using periodic conditions in the streamwise and
104 spanwise directions to reduce computational resource consumption and eliminate the sidewall effects. Based on
105 the experimental conditions, the dimensions of the domain are as follows: height ($H = 2h$) = 10 mm, where h is
106 the half-height of the channel, length (L) = 100 mm, and width (W) = 70 mm. For the mesh condition, the total
107 number of grid points is 29,970,336 ($404 \times 66 \times 562$ in the x -, y -, and z -directions, respectively). In detail, the
108 grid spacings in the streamwise and spanwise directions are $\Delta x^+ = 12.87$ and $\Delta z^+ = 6.47$, respectively, and non-
109 uniform grids are applied in the wall-normal direction. The first grid point away from the wall is at $\Delta y^+ = 0.54$,
110 and the maximum grid size is $\Delta y^+ = 12.84$ from the centerline of the channel.

111 **Table 1** lists the experimental and numerical conditions used in the present study along with those used in
112 previous studies (Oishi and Murai, 2014; Kim *et al.*, 2021), including the channel size. To generate turbulent
113 Couette flow in the channel, the velocity of the top wall in the channel (U_{wall}) is applied to obtain the same friction
114 velocity (u_τ) used in the previous studies; this facilitates a comparison of the bubble characteristics and drag
115 reduction performance in future investigations. All dimensionless numbers are obtained based on single-phase
116 flow conditions.

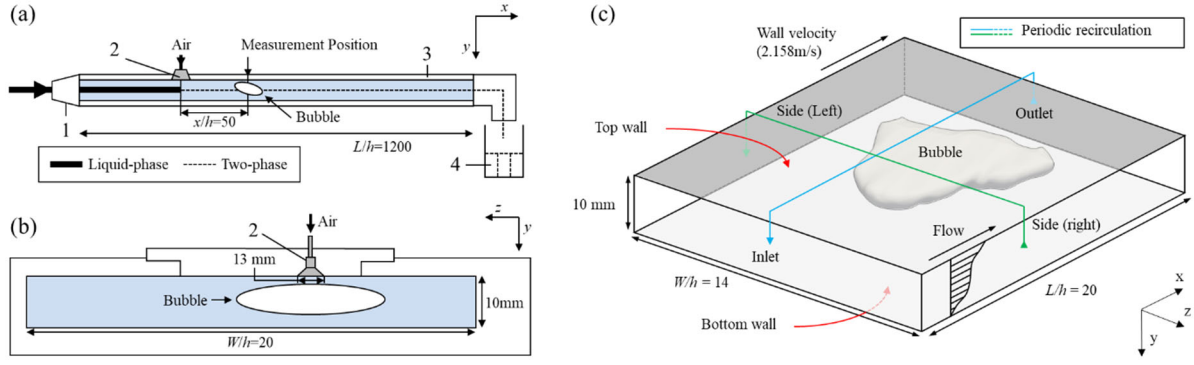
117

118 **Table 1** Comparison of the experimental and numerical conditions used in this study and in the literature.

	Oishi and Murai (2014)	Kim <i>et al.</i> (2021)	Present study
Flow condition	Poiseuille flow	Poiseuille flow	Couette flow
$L \times H \times W$ [mm]	$6000 \times 10 \times 100$	$100 \times 10 \times 70$	$100 \times 10 \times 70$
ρ [kg/m ³]	998.7	998.7	998.7
ν [m ² /s]	1.08×10^{-6}	1.08×10^{-6}	1.08×10^{-6}
U_{mean} [m/s]	1.0	1.039	1.11
U_{wall} [m/s]	–	–	2.16
Fr	3.19	3.31	3.54
Re	9260	9620	10278
Re_τ	260	260	260

119

120



121

122

123

124

Fig. 2 Schematic of the experimental and numerical conditions used in (a) Oishi and Murai (2014) and (b) the present study.

125 3. Numerical Methods

126 3.1 Volume of fluid method

127

128

129

130

131

132

133

134

135

136

137

138

139

140

141

142

143

144

The volume of fluid (VOF) method is a Eulerian volume tracking method in which a step α function is used to mark the volume fraction of the tracked phase in a control volume. The first advantage of the VOF method for the numerical simulation of large-sized bubbles is the conservation of mass by construction, which is crucial for addressing long-term calculations over a relatively large interfacial area. The second advantage is that the Eulerian framework of the VOF method allows the handling of large deformations and topological changes without requiring additional algorithms. This simplifies the results of bubble coalescence or breakup through a different field indicator distribution, especially when simulating large-sized bubbles that frequently show large deformations at the interface. The VOF method uses the continuity and momentum equations as the governing equations, as shown in Eqs. (1) and (2), respectively, as well as the transport equation of the volume fraction α , expressed as shown in Eq. (3). The advection equation of α enables the use of only one equation in the entire flow domain to describe the local properties, instead of applying a different set of equations to each phase. The volume fraction α can be averaged in each of the mesh cells, the interface between phases is found in cells where $0 < \alpha < 1$. Fluid properties, such as the density in the cells, can be calculated using α as a weighted average, as shown in Eq. (4).

$$\nabla \cdot \mathbf{u} = 0 \quad (1)$$

$$\frac{\partial \rho \mathbf{u}}{\partial t} + \rho \nabla \cdot (\mathbf{u} \mathbf{u}) = -\nabla p + \nabla \cdot \mathbf{T} + \rho \mathbf{f} + \rho \mathbf{f}_g \quad (2)$$

$$\frac{\partial \alpha}{\partial t} + \nabla \cdot (\alpha \mathbf{u}) = 0 \quad (3)$$

145 $\rho = \alpha \rho_{\text{water}} + (1 - \alpha) \rho_{\text{air}}$ (4)

146

147 The VOF method requires an additional surface capturing method to suppress the smearing of the
 148 volume fraction α from the interface cells. The *isoAdvector* method is a VOF-based geometric surface
 149 reconstruction technique that captures extremely sharp interfaces using the concept of isosurfaces. The volume
 150 fraction α in each cell C_i at time t can be expressed by the function $H(\mathbf{x}, t)$, as shown in **Eq. (5)**. Here, $H(\mathbf{x}, t)$ is
 151 an indicator field, as shown in **Eq. (6)** for time t and location \mathbf{x} . Additionally, the updated volume fraction α in
 152 each cell C_i from time t to $t + \Delta t$ can be formulated as described in **Eq. (7)**.

153

154 $\alpha_i(t) = \frac{1}{V_i} \int_{C_i} H(\mathbf{x}, t) dV$ (5)

155 $H(\mathbf{x}, t) \equiv \frac{\rho(\mathbf{x}, t) - \rho_{\text{air}}}{\rho_{\text{water}} - \rho_{\text{air}}}$ (6)

156 $\alpha_i(t + \Delta t) = \alpha_i(t) - \frac{1}{V_i} \sum_{j \in B_i} s_{ij} \int_t^{t+\Delta t} \int_{F_j} H(\mathbf{x}, \tau) \mathbf{u}(\mathbf{x}, \tau) \cdot d\mathbf{S} d\tau$ (7)

157

158 where B_i is the list of all faces F_j belonging to C_i , and the auxiliary factor s_{ij} is either +1 or -1 to ensure that the
 159 product $s_{ij}d\mathbf{S}$ is oriented outward from F_j .

160 The time integral of the second term on the right-hand side of **Eq. (8)** can be replaced by the total volume
 161 fraction transported across face j from time t to $t + \Delta t$, $\Delta V_j(t, \Delta t)$, as shown in **Eq. (9)**. The *isoAdvector* method
 162 requires the estimation of $\Delta V_j(t, \Delta t)$ using α_i and \mathbf{u}_i , as well as the constant volumetric face flux ϕ_j in **Eq. (9)**. A
 163 more detailed description of the *isoAdvector* method is available in Roenby *et al.* (2016) and Gamet *et al.* (2020).

164

165 $\Delta V_j(t, \Delta t) \equiv \int_t^{t+\Delta t} \int_{F_j} H(\mathbf{x}, \tau) \mathbf{u}(\mathbf{x}, \tau) \cdot d\mathbf{S} d\tau$ (8)

166 $\phi_j(t) = \int_{F_j} \mathbf{u}(\mathbf{x}, t) \cdot d\mathbf{S}$ (9)

167

168 Based on the above method, large-sized bubbles in turbulent Poiseuille channel flow can be modeled
 169 numerically, with good agreement between the numerical and experimental results (Oishi and Murai, 2014; Kim
 170 *et al.*, 2021).

171

172 **3.2 Numerical solvers and boundary conditions**

173 A numerical simulation was performed using the open-source computational fluid dynamics (CFD) package
 174 *OpenFOAM* v.1906. In this study, the *pimpleFoam* solver was used to generate a fully developed turbulent flow
 175 in the channel, while the *interIsoFoam* solver, which is used in the *isoAdvector* method as the interface-sharpening
 176 method, was used for two-phase flow. In short, this approach creates two divided cells within one cell containing
 177 the interface location; these cells occupy one or zero volume fractions, as controlled by the mean velocity of the
 178 cell. Further details, such as the verification of *interIsoFoam*, can be found in Kim *et al.* (2020, 2021).

179 All schemes used in this study provide second-order accuracy. The global time step was set to $2.0 \times$
 180 10^{-6} s to ensure that the Courant–Friedrichs–Lewy (CFL) number remained below 0.5—the interface CFL number
 181 was less than 0.1 in each simulation. It was maintained at approximately 0.4 in a previous study as the interface
 182 CFL number frequently increased sharply owing to the large and instantaneous deformation of bubbles during
 183 bubble breakup and coalescence. Both solvers use the *Pimple* algorithm for pressure-velocity coupling in a
 184 segregated manner, whereby a velocity field is computed to satisfy the continuity and momentum equations using
 185 an iterative procedure. **Table 2** lists the boundary conditions for the computational domain. At the inlet and outlet,
 186 periodic conditions are applied to the coupling conditions between them. These boundary conditions were also
 187 applied to the side boundaries. For the wall boundaries, the *NoSlip* condition is utilized to set the velocity to zero
 188 and generate a boundary layer. The *ConstantAlphaContactAngle* condition is additionally applied for two-phase
 189 flow to prevent bubble dispersion on the top wall. The numerical procedure can be divided into three stages to
 190 accommodate the required changes in the solvers and boundary conditions—that is, stage 1, which conducts fully
 191 developed turbulent Couette flow, stage 2, which conducts bubble injection and stabilization, and stage 3, which
 192 conducts turbulent channel flow with a single injected large-sized bubble. Further details regarding this numerical
 193 procedure are reported in Kim *et al.* (2020).

194

195 **Table 2** Boundary conditions and solvers used in each stage of the numerical procedure.

Term	Stage 1	Stage 2	Stage 3
Solver	<i>pimpleFoam</i>	<i>interIsoFoam</i>	
Top	<i>Wall velocity</i> (2.16 m/s)	<i>Wall velocity</i> (2.16 m/s), <i>ConstantAlphaContactAngle</i> (71°)	
Bottom	<i>NoSlip</i>	<i>NoSlip</i> , <i>ConstantAlphaContactAngle</i> (71°)	
Inlet/Outlet		<i>Cyclic</i> (Inlet ↔ Outlet)	
Side		<i>Cyclic</i> (Left ↔ Right)	

196 4. Modeling of turbulent Couette flow

197 **Figure 3** shows a schematic of the turbulent Couette flow generation in stage 1. The flow is driven by a pressure
198 gradient to reach a bulk velocity of 1.039 m/s, as shown in **Fig. 3(a)**, because it is easier to generate the initial
199 perturbation than only using wall velocity for the fully developed flow. Under this condition, a gap exists between
200 the pressure gradient region and the wall to generate the initial perturbation. After achieving the target mean
201 velocity and proper initial perturbation, the pressure gradient—which drives the channel flow—is removed, and
202 the velocity condition (2.16 m/s) of the top wall drives the flow, as shown in **Fig. 3(b)**. Finally, a turbulent Couette
203 flow is generated.

204 **Figure 4** shows the numerical results of the turbulent Couette flow. It was explored by examining the
205 profile of the dimensionless mean velocity in the streamwise direction $u^+ = (U_{\text{wall}} - u)/u_\tau$ and the root-mean-square
206 (RMS) velocity fluctuations in the streamwise and wall-normal directions, as shown in **Eq. (10)**, represented as a
207 function of the wall distance $y^+ = yu_\tau/\nu$, where y is the distance from the top wall. In addition, the dimensionless
208 Reynolds shear stress, represented as a function of the wall distance y/h , was examined.

209

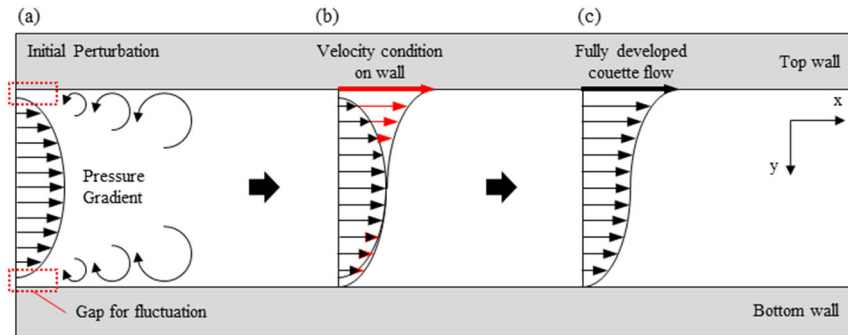
$$210 \quad u_{rms}^+ = \sqrt{u'^2} / u_\tau; \quad v_{rms}^+ = \sqrt{v'^2} / u_\tau \quad (10)$$

211

212 Results from two previous studies were compared with the results of the present study. The first set of
213 results was obtained from Oishi and Murai (2014), who used the same domain conditions as the present study, to
214 confirm the mean velocity profile and the difference in turbulent properties. The second set was obtained from
215 Avsarkisov *et al.* (2014), who investigated turbulent planar Couette flow in single-phase flow to determine
216 whether the turbulent properties were well simulated for Couette flow conditions. The mean velocity and RMS
217 velocity fluctuation in the wall-normal direction in the present study showed similar trends to those reported in
218 both studies. From the center of the channel ($y^+ \approx 300$), the mean velocity exhibited different trends from those of
219 Oishi and Murai (2014) because of the different flow conditions. The RMS velocity fluctuation in the streamwise
220 direction showed trends similar to those of both the previous studies below $y^+ = 50$. However, the present RMS
221 velocity fluctuation results were similar to but located above the results of Oishi and Murai (2014) from $y^+ = 50$,
222 but beneath those of Avsarkisov *et al.* (2014). This velocity fluctuation deviation in the streamwise and wall-
223 normal directions under turbulent Couette flow conditions could be expected to affect the Reynolds shear stress,
224 which exhibited different trends in the two previous studies. The present results approach those for turbulent
225 Couette flow, but some deviation remains, indicating that the momentum from the pressure gradient remained and

226 hindered the momentum transfer from the near-top wall to the bulk flow and bottom of the channel. Moreover,
 227 the current mesh condition was based on the flow conditions of Kim *et al.* (2021)—that is, the channel size could
 228 be insufficient to develop a coherent turbulent structure in turbulent Couette flow, as reported by Kawata and
 229 Tsukahara (2021). Meanwhile, deformation of the upper part of a large-sized bubble and the skin friction trends
 230 depended on the velocity gradient and shear rate near the viscous sublayer and buffer layer below $y^+ = 50$ ($y/h \approx$
 231 0.2), and present results accurately reproduced these regions. In addition, the size of a large-sized bubble is
 232 relatively larger than that of the turbulence length scale. Therefore, the local deformation at log-law region could
 233 be neglected, but we assume the entire trends are almost the same. In future work, the mesh condition should be
 234 investigated to improve the accuracy of the turbulent properties of turbulent Couette flow.

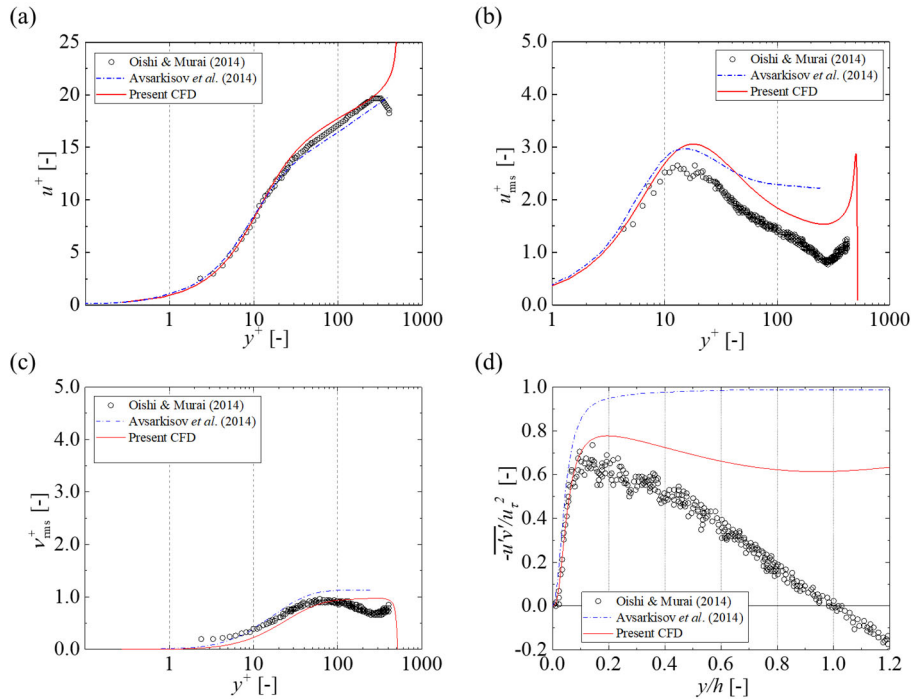
235



236

237 **Fig. 3** Sequence of turbulent Couette flow generation (a) Initial perturbation by the pressure gradient, (b) Change
 238 from pressure gradient to velocity condition on the wall, (c) Fully developed Couette flow.

239



240

241 **Fig. 4** Comparison of the turbulent properties between previous studies and this study. (a) Mean velocity, (b) RMS
 242 velocity fluctuation in the streamwise direction, (c) RMS velocity fluctuation in the wall-normal direction, and
 243 (d) Reynolds shear stress.

244 **5. Numerical Results and Discussion**

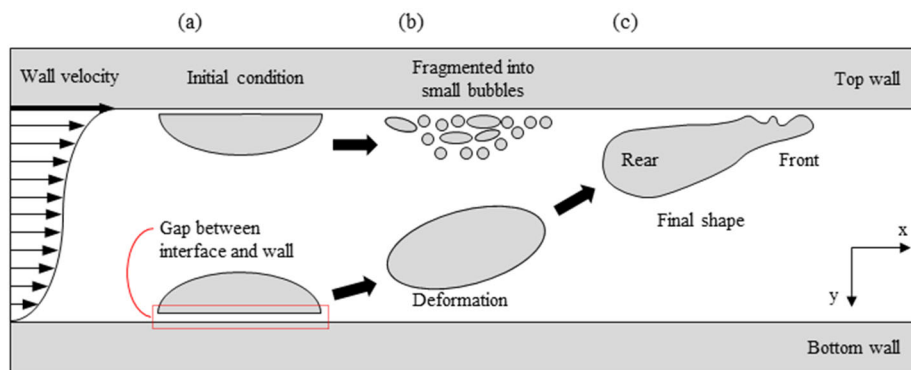
245 **5.1 Characteristics of the initial bubble**

246 In stage 2, the bubbles are injected using the *SetFields* function of *OpenFOAM*, which sets the scalar values of
 247 the fields in specific regions. To stabilize the bubble in the channel, an adjustable time step is used to maintain an
 248 interface CFL number below 0.4. When placing the bubble in the channel, as shown in **Fig. 5(a)**, a small gap is
 249 provided between the wall and the bubble interface (to represent a detached bubble); this saves computational
 250 resources by avoiding the simulation of the bubble detachment from the wall. The bubble is placed at the bottom
 251 of the channel because, when placed near the top wall, it is fragmented into small bubbles by the high shear,
 252 shown in the top panel of **Fig. 5(b)**. Consequently, the bubble shape can be successfully maintained, as shown in
 253 **Fig. 5(c)**.

254 Thus, further numerical simulations were performed on the three bubble cases, as shown in **Table 3** and
 255 **Fig. 6**, and the bubble properties were obtained before the initial breakup. There are two definitions of bubble
 256 velocity—that is, the traveling velocity of the bubble $U_{tra.}$ and the relative velocity $U_{rel.}$ for the top-wall velocity,
 257 where $U_{rel.} = U_{wall} - U_{tra.}$. Thus, the Weber numbers, $We_{tra.}$ and $We_{rel.}$, were obtained using these two velocities.

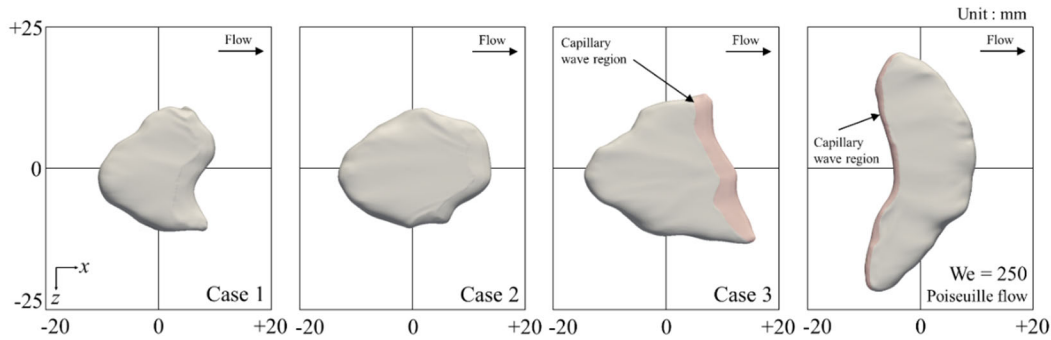
258 The cases in the present study were for $We_{tra.}$ within 200–300, where the skin-friction drag reduction in
 259 the secondary flow and the middle of the liquid film were observed as in Kim *et al.* (2021). The bubbles over
 260 $We_{tra.} \approx 300$ were not included because they showed breakup patterns different from those of the present study,
 261 making it difficult to categorize the deformation characteristics. Consequently, the cases of the present study were
 262 established based on $We_{tra.}$ in the range of 200–300, each case having a different bubble volume. As expected from
 263 **Fig. 1**, the capillary wave region—which extends from the top of the liquid film to the edge of the bubble (colored
 264 red in **Fig. 6**)—is formed at the front of the bubble, while the rear shape of the individual bubble is round and
 265 arched. The present cases exhibit frequent oscillation and wider capillary wave region areas than those in the
 266 reference cases of Kim *et al.* (2021).

267



268

269 **Fig. 5** Schematic of bubble injection in the channel. (a) Initial condition of a bubble when placed near the top and
 270 bottom, (b) Intermediate condition of bubble deformation according to the initial placement, and (c) Final shape
 271 of a bubble when placed at the bottom of the channel



272
 273
 274

Fig. 6 Top view of the initial bubble shape for each case.

275 **Table 3** Bubble parameters. The equivalent bubble diameter d_e is calculated from the bubble volume V_b .

		Case 1	Case 2	Case 3	Poiseuille flow (Kim <i>et al.</i> 2021)
Bubble volume (V_{bubble}) [mm ³]		1463.3	1912.2	2167.5	2070.5
Equivalent diameter ($D_{\text{equiv.}}$) [mm]		14.09	15.40	16.06	15.82
	$U_{\text{tra.}}$ [m/s]	1.075	1.083	1.112	1.054
Bubble velocity	$U_{\text{tra.}} / U_{\text{mean}}$	0.968	0.976	1.002	1.015
	$U_{\text{rel.}}$ [m/s]	1.085	1.077	1.048	-
	$U_{\text{rel.}} / U_{\text{mean}}$	0.977	0.970	0.944	-
Weber number	$We_{\text{tra.}} = \rho U_{\text{tra.}}^2 D_{\text{equiv.}} / \sigma$	232	258	283	250
	$We_{\text{rel.}} = \rho U_{\text{rel.}}^2 D_{\text{equiv.}} / \sigma$	237	255	252	-

276

277 5.2 Shape evolution and deformation characteristics of a large-sized bubble

278 **Figures 7–9** show the top views of the time-domain bubble evolution for the different cases. The bubble shape
 279 could not be visualized in a uniform time interval as the bubble crosses the cyclic boundary conditions in the
 280 streamwise and spanwise directions and is thus divided into several parts. Consequently, the images were obtained
 281 when the bubble was located near the center or not hanging over these boundaries. Although it was difficult to
 282 determine the bubble dynamics with respect to bubble size, bubble deformation could be categorized as follows:

- 283 a) The initial state of the bubble prior to deformation, corresponding to Case 1 (0–167, 351, 410, 621,
 284 671 ms), Case 2 (0, 59, 270, 369, 432 ms), and Case 3 (0, 500, 693 ms). The front side of the bubble
 285 is irregular, with a high curvature on the tip in the spanwise direction.
- 286 b) After the initial state, ligaments develop from the span edge of the front side of the bubble. Generally,
 287 the ligament head grows from the front and outer sides in the spanwise direction. These ligaments
 288 develop from both sides for Case 1 (261, 288 ms), Case 2 (180, 270 ms), and Case 3 (63, 122, 522–

289 612 ms), when the front side of the bubble is aligned perpendicular to the streamwise direction. These
 290 ligaments exhibit an imbalance between them, and smaller ligaments are frequently suppressed. By
 291 contrast, a one-direction development of the ligament can be observed in Case 1 (410–536 ms) and
 292 Case 2 (95–203, 396, 486–572 ms) when the front side of the bubble is tilted in the streamwise
 293 direction.

294 c) The ligament tips exhibit pinch-off and breakup, as in Case 1 (297–320, 540, 554 ms), Case 2 (243
 295 ms), and Case 3 (243, 252, 612–666 ms). Daughter bubbles are generated and detach from the main
 296 bubbles. These daughter bubbles are typically small, considering that the major bubbles do not affect
 297 the total volume, as shown in **Table 4**, where the volume ratios of the daughter bubbles are distributed
 298 near zero. After breakup, the ligament bases experience splash-back, and the center of the air mass
 299 shifts to the center of the bubble again.

300 d) Not all of the ligaments experience splash-back after breakup. A ligament that is larger than one
 301 opposite of it suppresses its development. Eventually, the center of the air mass shifts to the ligament
 302 side such that the main bubble part shrinks, and the ligament expands for Case 2 (243–338 ms) and
 303 Case 3 (252–383 ms). This situation occurs without splitting, as in Case 2 (486–572 ms).

304 e) After the breakup from the tip of the ligaments or the shifting of the center of the air mass to the
 305 ligament side, the bubble shape deforms for shape stabilization, as in Case 1 (351, 410, 621, 671 ms),
 306 Case 2 (270, 369, 432 ms), and Case 3 (500, 693 ms). The bubble rotates from the streamwise
 307 direction owing to the direction of the development of a relatively large ligament. From this state,
 308 one direction of ligament development is frequently observed.

311 **Table 4** Volume ratio of daughter bubbles, V_{daughter} , and major bubble, V_{major} . V_{total} is the total volume of the bubble
 312 before each breakup.

	Time [ms]	$V_{\text{daughter}} / V_{\text{total}} [-]$	$V_{\text{major}} / V_{\text{total}} [-]$
Case 1	297	0.04×10^{-2}	99.96×10^{-2}
	320	0.09×10^{-2}	99.91×10^{-2}
	554	0.05×10^{-2}	99.95×10^{-2}
Case 2	243	0.09×10^{-2}	99.91×10^{-2}
	252	0.91×10^{-2}	99.09×10^{-2}
Case 3	468	0.02×10^{-2}	99.98×10^{-2}
	648	4.11×10^{-2}	95.89×10^{-2}
	666	5.39×10^{-2}	94.61×10^{-2}

313

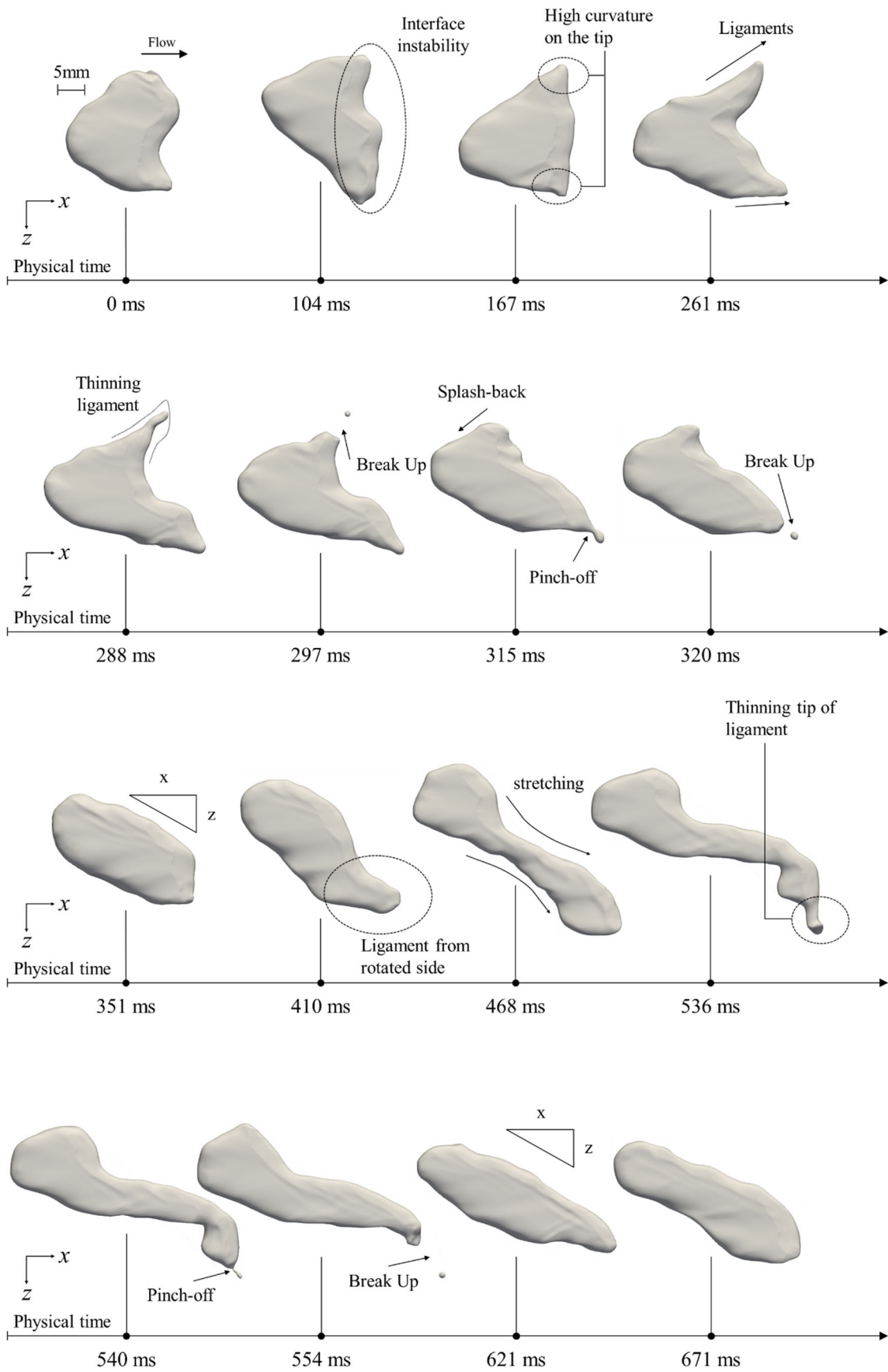


Fig. 7 Top view of the bubble shape evolution for case 1

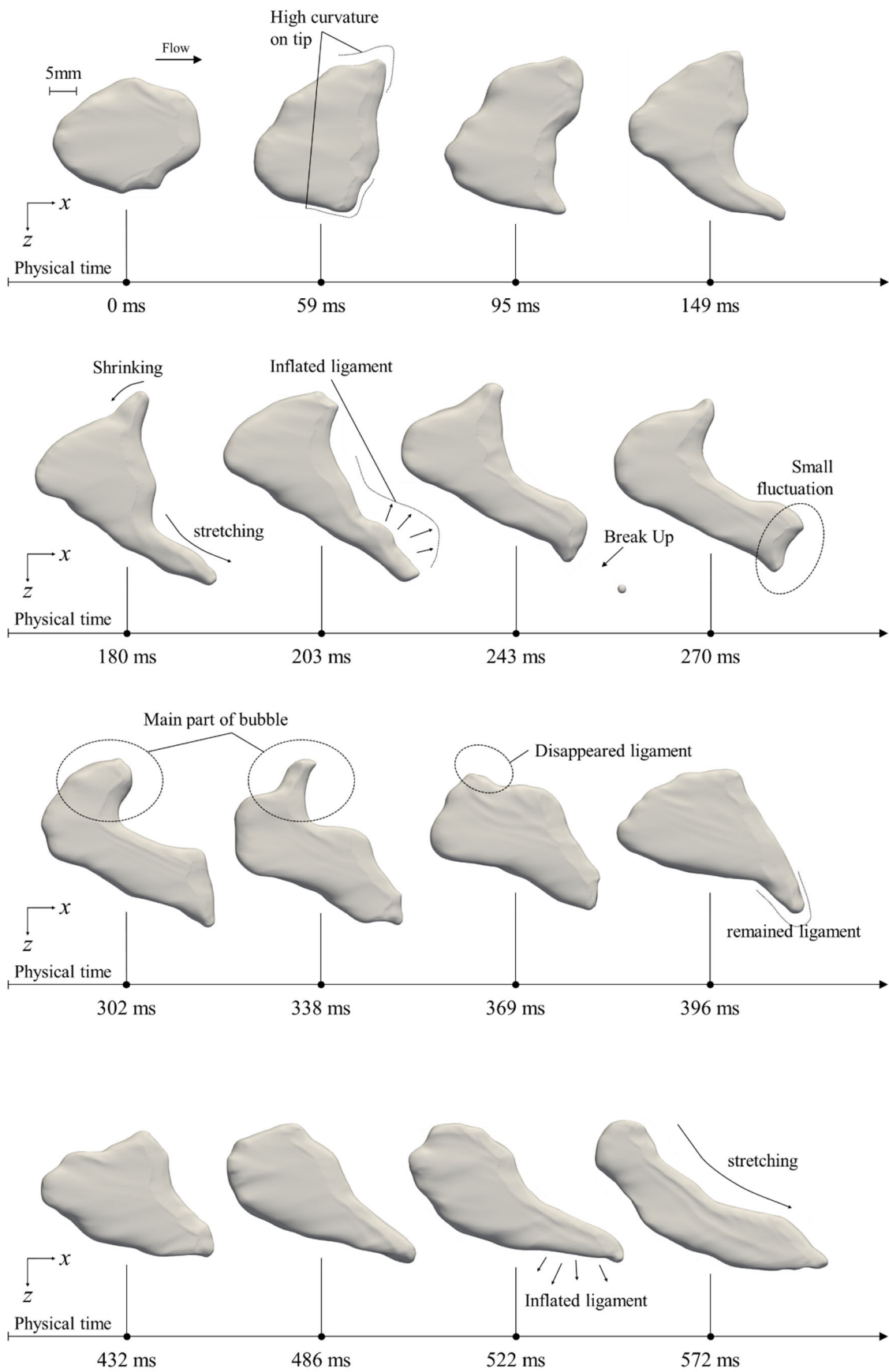


Fig. 8 Top view of the bubble shape evolution for case 2

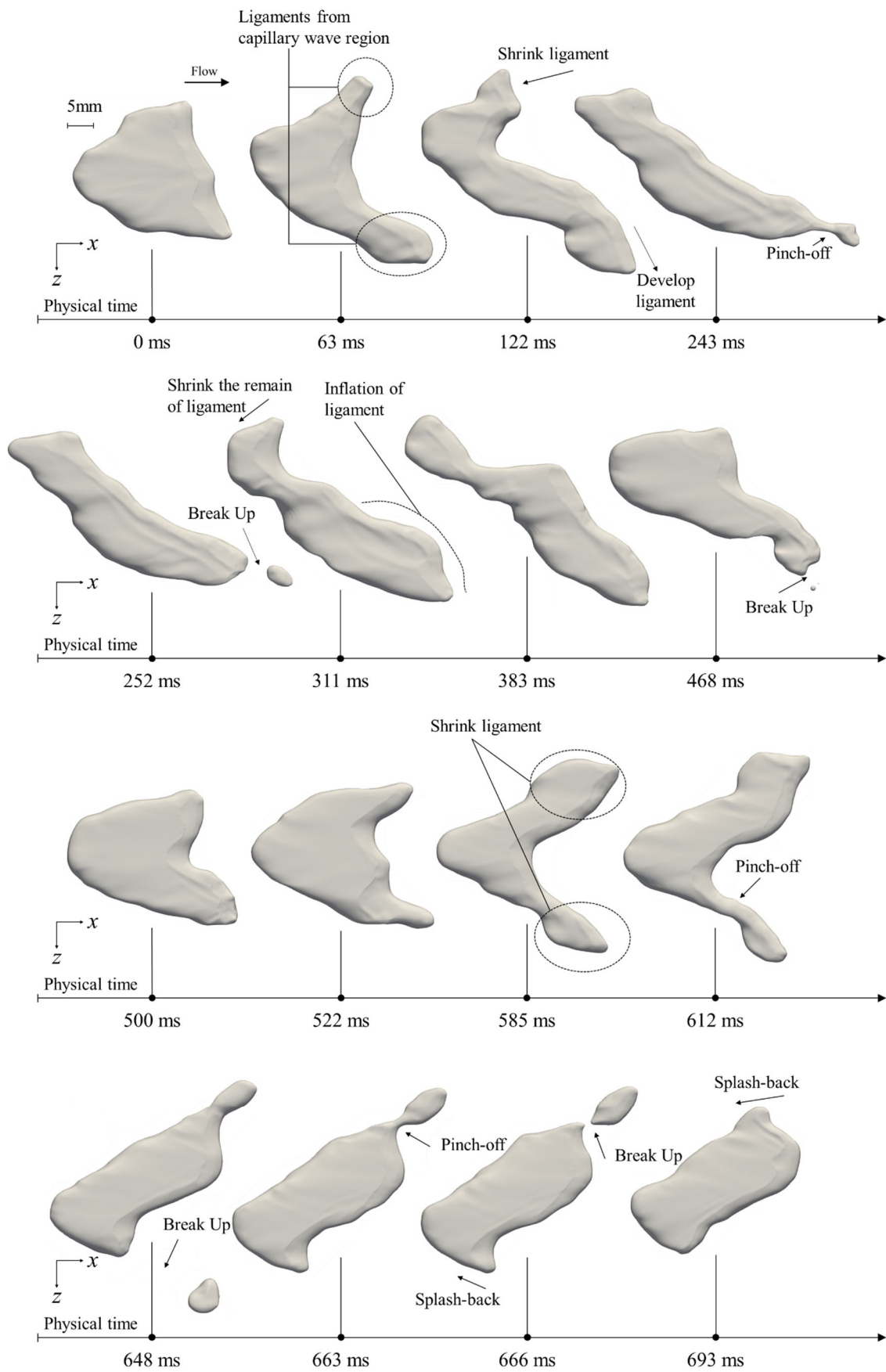


Fig. 9 Top view of the bubble shape evolution for case 3

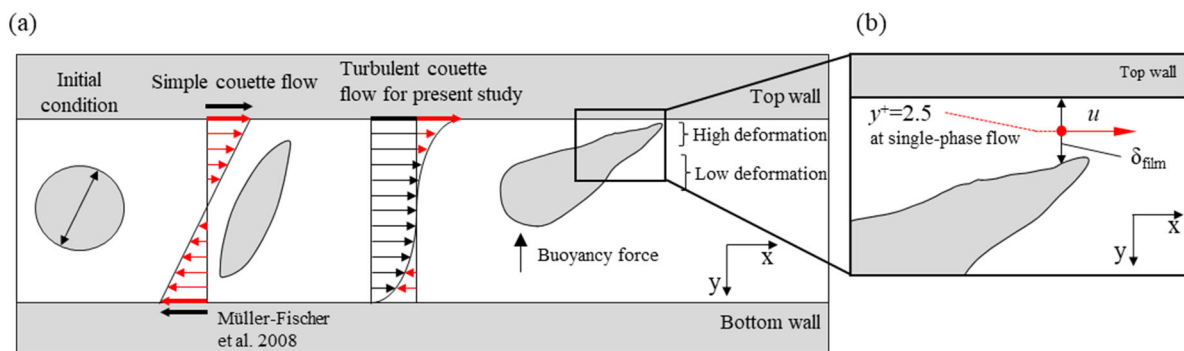
321 **5.2 Relationship between liquid film thickness and velocity ratio**

322 In this study, we categorized several sequences of the deformation of large-sized bubbles, and the development
323 of ligaments in both directions was confirmed at a Weber number of approximately 300 in turbulent Poiseuille
324 flow, as described by Kim *et al.* (2021). However, in one direction, ligament and inflation were not observed at
325 all, this deformation being considered to be present for large-sized bubbles for the current cases in turbulent
326 Couette flow. Thus, the velocity field around the bubble was investigated based on our knowledge of bubble
327 deformation in Couette flow, as shown in **Fig. 10(a)**.

328 The bubble in laminar Couette flow deforms linearly; thus, the bubble in turbulent Couette flow exhibits
329 high deformation at its tip owing to the exponential change in velocity near the wall. Consequently, the ligament
330 at the tip may be affected by the velocity around the bubble, while the bottom of the bubble does not reach the
331 bottom of the channel owing to its buoyancy in the wall-normal direction. Therefore, the relationship between the
332 velocity and liquid film thickness was investigated, as shown in **Fig. 10(b)**; the velocity in single-phase flow was
333 obtained at $y^+ = 2.5$.

334 **Figures 11–13** show dimensionless velocity and liquid film thickness for each case. The dimensionless
335 velocity was obtained by dividing the instantaneous velocity by the mean velocity of the single-phase flow at y^+
336 $= 2.5$, while the dimensionless liquid film thickness was obtained by dividing the liquid film thickness by the half-
337 height of the channel. As shown, the high-velocity region of the ligaments is eventually inflated and stretched for
338 all cases, while the main parts of the bubble gradually shrink. Consequently, the inflating and shrinking of each
339 part of the bubbles is strongly associated with the high flow field in the liquid film. Moreover, the liquid film
340 thickness of these regions are lower than those of other regions.

341



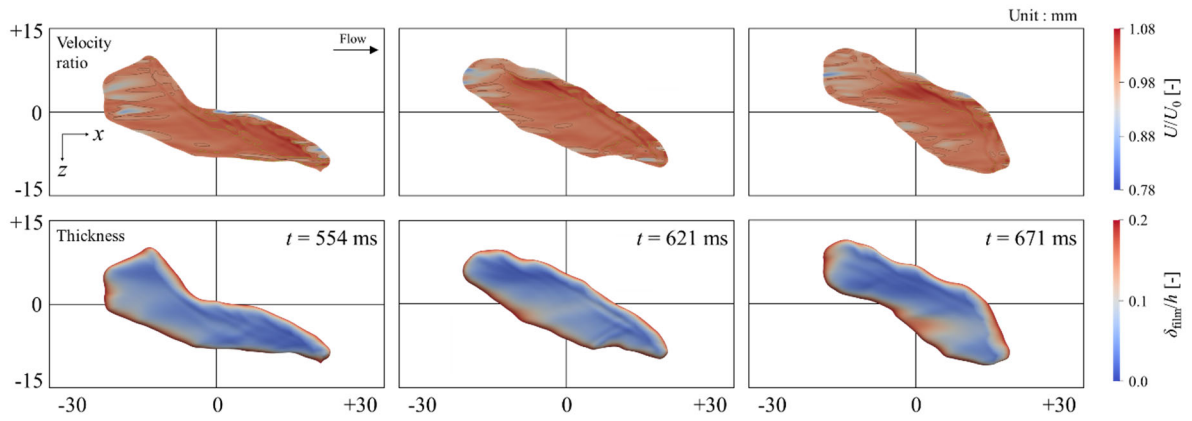
342

343

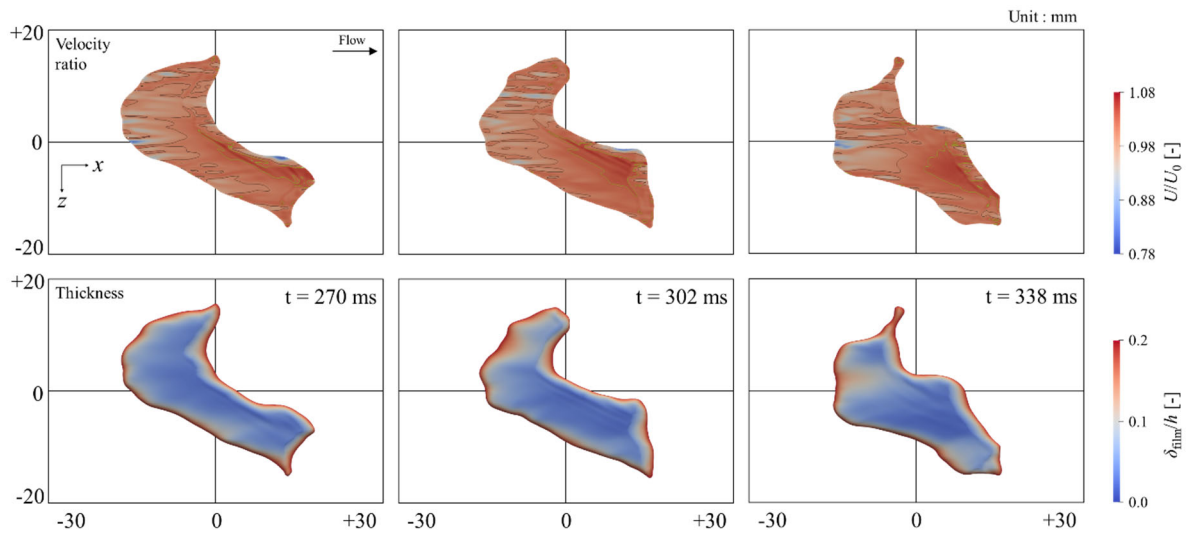
344 **Fig. 10(a)** Illustration of bubble deformation at laminar (Müller-Fischer *et al.*, 2008) and turbulent Couette flow,
345 (b) Schematic view of liquid film thickness and the height where velocity is obtained.

346

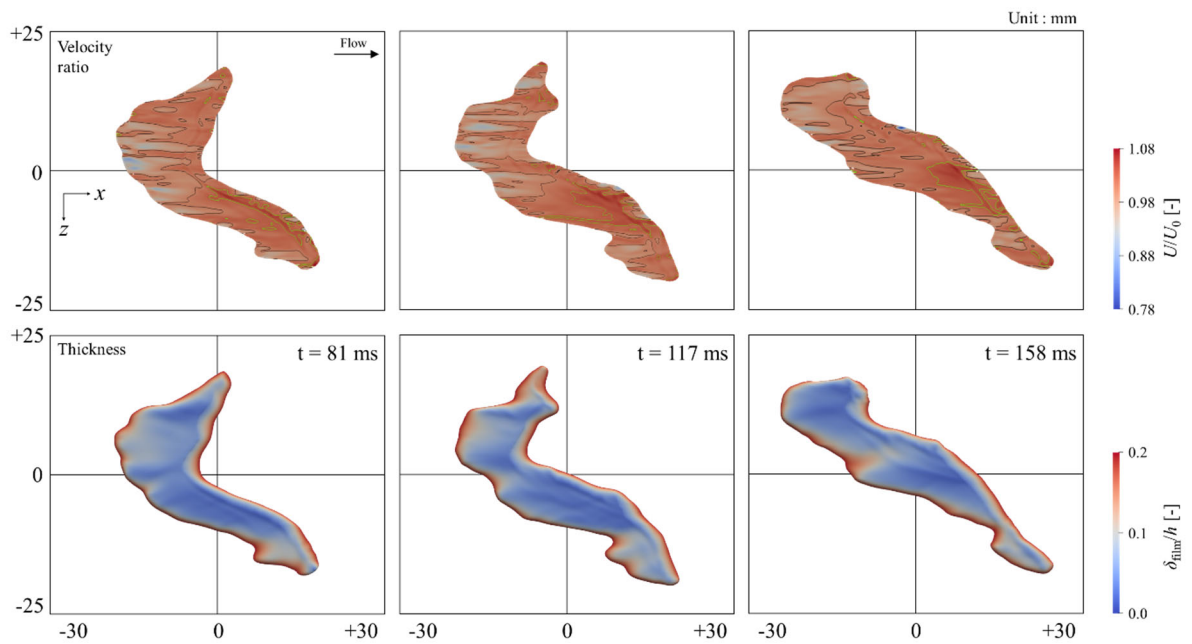
347



348
349
350 **Fig. 11** Dimensionless velocity and liquid film thickness for case 1

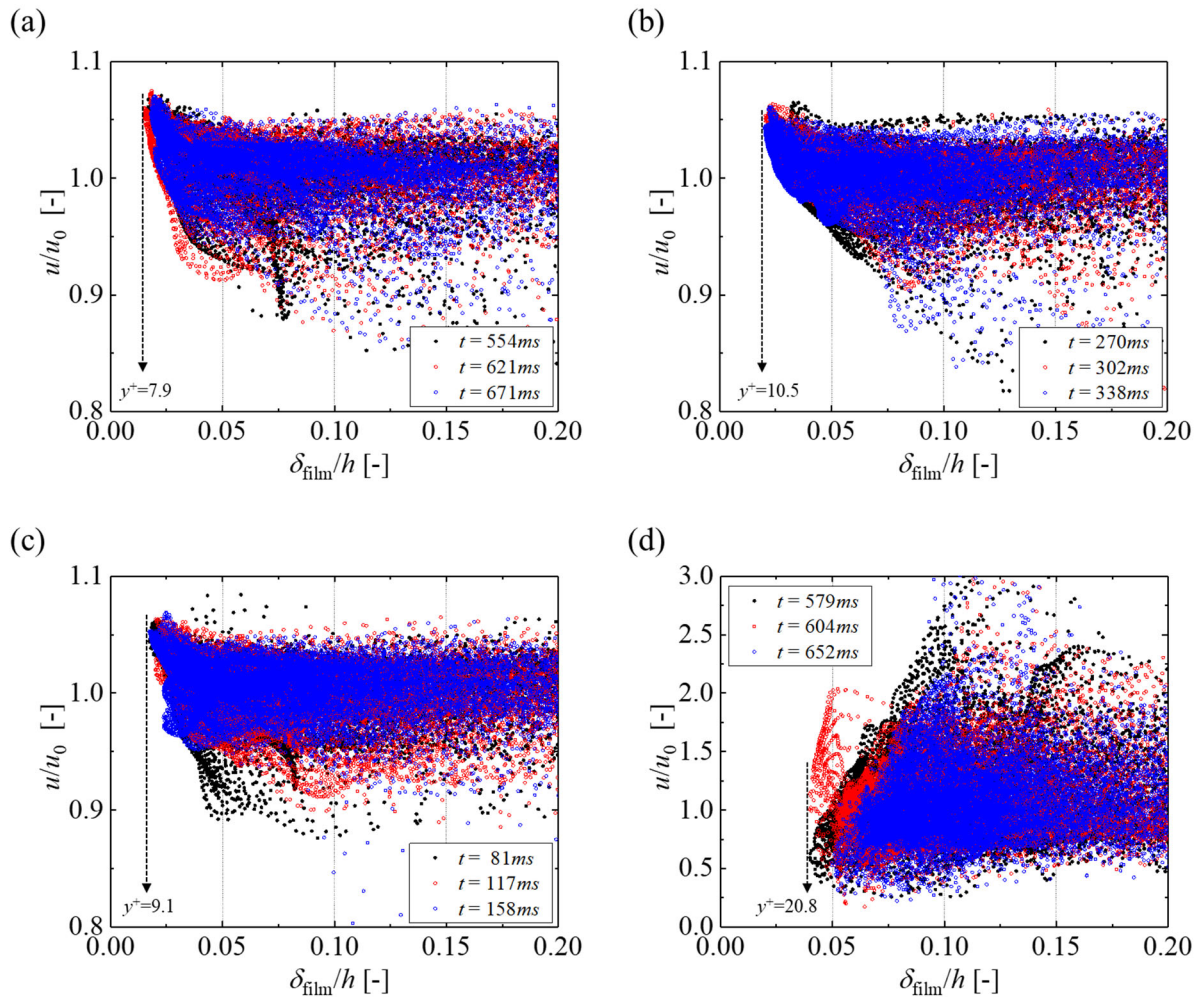


351
352
353 **Fig. 12** Dimensionless velocity and liquid film thickness for case 2



354
355
356 **Fig. 13** Dimensionless velocity and liquid film thickness for case 3

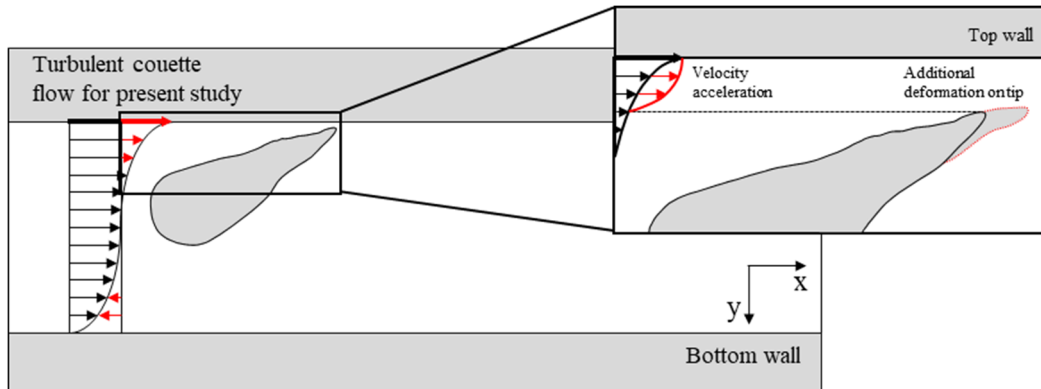
357 **Figure 14** shows the relationship between dimensionless velocity and liquid film thickness. The results
 358 for each case are compared with the reference case, obtained at a Weber number of 250 in Poiseuille flow.
 359 Typically, the dimensionless velocity in Couette flow is distributed widely between 0.8 and 1.05. Meanwhile,
 360 there is variation in the time and bubble cases—that is, the data is concentrated, with the dimensionless velocity
 361 being inversely proportional to the specific liquid film thickness. The dimensionless velocity increases to
 362 approximately 1.05 below $\delta_{\text{film}}/h = 0.05$. In the reference case, the distributions are the reverse of those in Couette
 363 flow; however, δ_{film}/h is not above 0.05, and exhibits no concentrated trends near $\delta_{\text{film}}/h = 0.05$. Thus, the velocity
 364 increase in this region and the thinning of the liquid film in Couette flow are considered to cause additional
 365 deformation on the tip, similar to the development of the ligament, as shown in **Fig. 15**.
 366



367
 368 **Fig. 14** Scatter plots of the relationship between dimensionless velocity and liquid film thickness. (a) Case 1, (b)
 369 Case 2, (c) Case 3, and (d) Reference case, $We = 250$ in Kim *et al.* (2021).
 370

371
 372

373



374

375

376

Fig. 15 Velocity acceleration on the liquid film and additional deformation of the tip of the bubble.

377 **6. Conclusions**

378 In this study, a numerical flow visualization of a single large-sized bubble in a turbulent Couette flow was
379 performed. As expected for such a bubble, the representative bubble shape characteristics—such as the liquid film
380 and the capillary wave—were formed in a direction opposite to that in the Poiseuille flow. **Figure 16** shows the
381 physical bubble deformation mechanism in turbulent Couette flow, which is described in detail below.

- 382 i) In the initial state, the bubble shows a relatively round shape on the rear side and interface instability
383 on the front side with a high tip curvature in the spanwise direction.
- 384 ii) Two types of deformation occur on the front side (ligament)—that is, the first occurs in both
385 directions when the front side is aligned perpendicular to the streamwise direction and the formation
386 of relatively small ligaments is suppressed; the second occurs when the front side is tilted relative to
387 the streamwise direction, this condition occurs frequently and is maintained even when the tip breaks.
- 388 iii) A change of the center of gravity (CG) of the bubble could be observed after the one-direction
389 ligament development. This ligament is sometimes larger than the main part of the bubble, causing
390 shrinkage of the main bubble.
- 391 iv) Pinch-off and breaking of the ligament occur when it is sufficiently developed. The tip of the
392 ligament frequently breaks and shrinks quickly owing to splash-back. Meanwhile, the large ligament
393 arising from the change in the bubble CG shows only a small fluctuation on the breakup surface and
394 maintains its shape.
- 395 v) Deformation to a stable state (similar to the initial stage) occurs after sequences (iii) and (iv).
396 Interestingly, in most cases, the front side is tilted in a certain direction because of the imbalance in

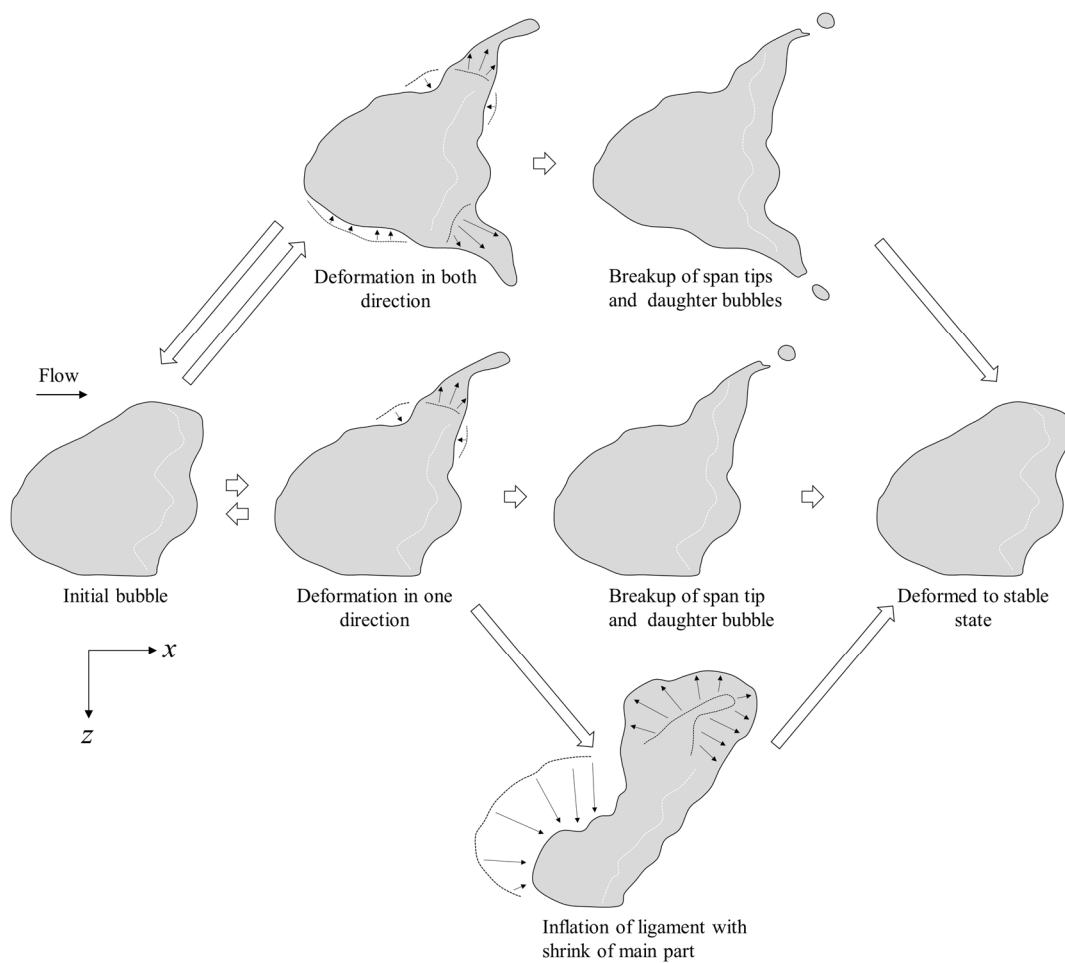
397 ligament size and change in the bubble CG. Consequently, this condition quickly changes to sequence

398 (ii).

399 Based on this bubble deformation sequence, we observed the development of ligaments in one direction
400 and the inflation of ligaments with shrinkage of the main part of the bubble. This bubble deformation was
401 dominated by the displacement of the main part of the bubble, which experienced an increase in velocity greater
402 than that during single-phase flow from the liquid film region. From the scatter plot depicting the relationship
403 between the dimensionless velocity and liquid film thickness, it is clear that the increase in velocity occurred
404 below $\delta_{\text{film}}/h = 0.05$.

405 The bubble cases in this study were limited to a Weber number range of 200–300. Thus, in future work,
406 numerical simulations should be performed for Weber numbers beyond these limits—that is, below 200 and above
407 300—to generalize the bubble deformation mechanism in turbulent Couette flow.

408



409

410 **Fig. 16** Schematic of the large-sized bubble deformation sequence in turbulent Couette flow.

411

412 **Acknowledgments**

413 This work was supported by the MEXT Doctoral program for the Data-Related InnoVation Expert Hokkaido
414 University (D-DRIVE-HU) program; the high-performance computing project (hp200223, hp210160); the
415 Fundamental Research Development Association for Shipbuilding and Offshore (REDAS); and the F3
416 Engineering Education and Research Center, Faculty of Engineering, Hokkaido University. The authors thank Dr.
417 Yuichi Murai, Hokkaido University, for his valuable discussions on bubble dynamics.

418
419 **References**

- 420
421 Andreolli A, Quadrio M, and Gatti D (2015) Global energy budgets in turbulent Couette and Poiseuille flows. *J*
422 *Fluid Mech* 924:A25 <https://doi.org/10.1017/jfm.2021.598>
- 423 Avsarkisov V, Hoyas S, Oberlack M, and García-Galache JP (2014) Turbulent plane Couette flow at moderately
424 high Reynolds number. *J Fluid Mech* 751:R1 <https://doi.org/10.1017/jfm.2014.323>
- 425 Fokoua NG, Gabillet C, Aubert A, Colin C (2015) Effect of bubble's arrangement on the viscous torque in bubbly
426 Taylor–Couette flow. *Phys Fluids* 27:034105 <https://doi.org/10.1063/1.4915071>
- 427 Fukuda K, Tokunaga J, Nobunaga T, Nakatani T, Iwasaki T, and Kunitake Y (1999) Frictional drag reduction
428 with air lubricant over super water repellent surface (2nd report): Resistance tests of tanker and high length-
429 to-beam ratio ship models. *J Soc NA Jpn* 186:73-81. https://doi.org/10.2534/JJASNAOE1968.1999.186_73
- 430 Gamet L, Scala M, Roenby J, Scheufler H, Pierson J-L (2020) Validation of volume-of-fluid OpenFOAM®
431 isoAdvector solvers using single bubble benchmarks. *Comput Fluids* 213: 104722
432 <https://doi.org/10.1016/j.compfluid.2020.104722>
- 433 Hinze JO (1955) Fundamentals of the hydrodynamic mechanism of splitting in dispersion processes. *AIChE J*
434 1:289–295 <https://doi.org/10.1002/aic.690010303>
- 435 Johansen J, Castro AM, and Carrica P (2010) Full-scale two-phase flow measurements on Athena research vessel.
436 *Int J Multiphase Flow* 36:720–737 <https://doi.org/10.1016/j.ijmultiphaseflow.2010.05.002>
- 437 Kawata T and Tsukahara T (2021) Scale interactions in turbulent plane Couette flows in minimal domains. *J Fluid*
438 *Mech* 991:A55 <https://doi.org/10.1017/jfm.2020.1063>
- 439 Katsui T, Okamoto Y, Kasahara Y, Shimoyama N, Iwasaki Y, Soejima S, and Hirayama A (2003) A study of air
440 lubrication method to reduce frictional resistance of ship. *J Kansai Soc NA Jpn* 239:45–53 (in Japanese)
441 https://doi.org/10.14856/jksna.2003.239_45
- 442 Kim SW, Oshima N, Murai Y, and Park HJ (2020) Numerical investigation of a single intermediate-sized bubble
443 in horizontal turbulent channel flow. *J Fluid Sci Technol* 15(3):JFST0020
444 <https://doi.org/10.1299/jfst.2020jfst0020>
- 445 Kim SW, Oshima N, Murai Y, and Park HJ (2021) Direct numerical simulation of frictional drag modulation in
446 horizontal channel flow subjected to single large-sized bubble injection. *Int J Multiphase Flow* 145:103838
447 <https://doi.org/10.1016/j.ijmultiphaseflow.2021.103838>
- 448 Kodama Y, Kakugawa A, Takahashi T, and Kawashima H (2000) Experimental study on microbubbles and their
449 applicability to ships for skin friction reduction. *Int J Heat Fluid Flow* 21(5):582–588
450 [https://doi.org/10.1016/S0142-727X\(00\)00048-5](https://doi.org/10.1016/S0142-727X(00)00048-5)
- 451 Madavan NK, Deutsch S, and Merkle CL (1984) Reduction of turbulent skin friction by microbubbles. *Phys Fluids*
452 27(2):356–363. <https://doi.org/10.1063/1.864620>
- 453 Mäkiharju S A, Elbing BR, Wiggins A, Schinasi S, Vanden-Broeck J-M, Perlin M, Dowling DR, and Ceccio SL
454 (2013) On the scaling of air entrainment from a ventilated partial cavity. *J Fluid Mech* 732:47–76
455 <https://doi.org/10.1017/jfm.2013.387>
- 456 McCormick ME and Bhattacharyya R (1973) Drag reduction of a submersible hull by electrolysis. *Nav Eng J*
457 85(2):11–16 <https://doi.org/10.1111/j.1559-3584.1973.tb04788.x>
- 458 Merkle CL and Deutsch S (1992) Microbubble drag reduction in liquid turbulent boundary layers. *ASME Appl*
459 *Mech Rev* 45(3):103–127 <https://doi.org/10.1115/1.3119751>

460 Murai Y, Fujii H, Tasaka Y, and Takeda Y (2006) Turbulent bubbly channel flow investigated by ultrasound
461 velocity profiler. *J Fluid Sci Technol* 1(1):12-23 <https://doi.org/10.1299/jfst.1.12>

462 Murai Y, Fukuda H, Oishi Y, Kodama Y, and Yamamoto F (2007) Skin friction reduction by large air bubbles in
463 a horizontal channel flow. *Int J Multiphase Flow* 33(2):147–163.
464 <https://doi.org/10.1016/j.ijmultiphaseflow.2006.08.008>

465 Murai Y, Oiwa H, and Takeda Y (2008) Frictional drag reduction in bubbly Couette-Taylor flow. *Phys Fluids*
466 20(3):034101 <https://doi.org/10.1063/1.2884471>

467 Murai Y (2014) Frictional drag reduction by bubble injection. *Exp Fluids* 55:1773 [https://doi.org/10.1007/s00348-](https://doi.org/10.1007/s00348-014-1773-x)
468 014-1773-x

469 Murai Y, Tasaka Y, Oishi Y, and Takeda Y (2018) Modal switching of bubbly Taylor–Couette flow investigated
470 by particle tracking velocimetry. *Exp Fluids* 59:164 <https://doi.org/10.1007/s00348-018-2620-2>

471 Müller-Fischer N, Tobler P, Dressler M, Fischer P, and Windhab EJ (2008) Single bubble deformation and
472 breakup in simple shear flow. *Exp Fluids* 45:917–926. <https://doi.org/10.1007/s00348-008-0509-1>

473 Oishi Y and Murai Y (2014) Horizontal turbulent channel flow interacted by a single large bubble. *Exp Therm*
474 *Fluid Sci* 55:128–139. <https://doi.org/10.1016/j.expthermflusci.2014.02.022>

475 Orlandi P, Bernardini M, and Pirozzoli S (2015) Poiseuille and Couette flows in the transitional and fully turbulent
476 regime. *J Fluid Mech* 770:424–441 <https://doi.org/10.1017/jfm.2015.138>

477 Park HJ, Oishi Y, Tasaka Y, Murai Y, and Takeda Y (2009) Turbulent shear control with oscillatory bubble
478 injection. *J Phys: Conf Ser* 147:012037 <https://doi.org/10.1088/1742-6596/147/1/012037>

479 Park HJ, Tasaka Y, Oishi Y, and Murai Y (2015) Drag reduction promoted by repetitive bubble injection in
480 turbulent channel flows. *Int J Multiphase Flow* 75:12–25
481 <https://doi.org/10.1016/j.ijmultiphaseflow.2015.05.003>

482 Park HJ, Oishi Y, Tasaka Y, and Murai Y (2016) Void waves propagating in the bubbly two-phase turbulent
483 boundary layer beneath a flat-bottom model ship during drag reduction. *Exp Fluids* 57:178
484 <https://doi.org/10.1007/s00348-016-2268-8>

485 Park HJ, Tasaka Y, and Murai Y (2018) Bubbly drag reduction accompanied by void wave generation inside
486 turbulent boundary layers. *Exp Fluids* 59:166 <https://doi.org/10.1007/s00348-018-2621-1>

487 Park HJ, Tasaka Y, and Murai Y (2019) Bubbly drag reduction investigated by time-resolved ultrasonic pulse
488 echography for liquid films creeping inside a turbulent boundary layer. *Exp Therm Fluid Sci* 103:66–77
489 <https://doi.org/10.1016/j.expthermflusci.2018.12.025>

490 Park HJ, Tasaka Y, and Murai Y (2022) Spatial development of single void pulse in a horizontal turbulent bubbly
491 channel flow investigated by a time-resolved two-laser measurement. *Int J Multiphase Flow* 146:103867
492 <https://doi.org/10.1016/j.ijmultiphaseflow.2021.103867>

493 Roenby J, Bredmose H, and Jasak H (2016) A computational method for sharp interface advection. *R Soc Open*
494 *Sci* 3:160405 <https://doi.org/10.1098/rsos.160405>

495 Sanders WC, Winkel ES, Dowling DR, Perlin M, and Ceccio SL (2006) Bubble friction drag reduction in a high-
496 Reynolds-number flat-plate turbulent boundary layer. *J Fluid Mech* 552:353–380.
497 <https://doi.org/10.1017/S0022112006008688>

498 Tanaka T, Park HJ, Tasaka Y, and Murai Y (2020) Spontaneous and artificial void wave propagation beneath a
499 flat-bottom model ship. *Ocean Eng* 214:107850 <https://doi.org/10.1016/j.oceaneng.2020.107850>

500 Tanaka T, Oishi Y, Park HJ, Tasaka Y, Murai Y, and Kawakita C (2021) Repetitive bubble injection promoting
501 frictional drag reduction in high-speed horizontal turbulent channel flows. *Ocean Eng* 239:109909
502 <https://doi.org/10.1016/j.oceaneng.2021.109909>